

The sound from mixing layers simulated with different ranges of turbulence scales

Randall R. Kleinman and Jonathan B. Freund

Department of Mechanical Science and Engineering and Department of Aerospace Engineering, University of Illinois at Urbana-Champaign, Urbana, Illinois 61801, USA

(Received 30 November 2007; accepted 4 May 2008; published online 31 October 2008)

The role of turbulence scales in generating far-field sound in free shear flows is studied via direct numerical simulations of temporally developing, Mach 0.9 mixing layers. Four flows were simulated, starting from the same initial conditions but with Reynolds numbers that varied by a factor of 12. Above momentum thickness Reynolds number $Re_{\delta_m} \approx 300$, all the mixing layers radiate over 85% of the acoustic energy of the apparently asymptotically high-Reynolds-number value that we are able to compute. Turbulence energy and pressure wavenumber spectra show the expected Reynolds number dependence; the two highest Reynolds number simulations show evidence of an inertial range and Kolmogorov scaling at the highest wavenumbers. Far-field pressure spectra all decay much more rapidly with wavenumber than the corresponding near-field spectra and show significantly less sensitivity to Reynolds number. Low wavenumbers account for nearly all of the radiated acoustic energy. Far-field streamwise wavenumber pressure spectra scale well with the layer momentum thickness, consistent with the insensitivity to Reynolds number of the largest turbulence structures. At higher wavenumbers the streamwise spectra scale best with the Taylor microscale. Interestingly, none of the spanwise far-field pressure spectra scale well with momentum thickness despite doing so in the near-field turbulence. Instead they scale well at all wavenumbers with the turbulence microscale. Implications of these results for large-eddy simulation of jet noise are discussed. © 2008 American Institute of Physics. [DOI: 10.1063/1.3005823]

I. INTRODUCTION

The radiated sound spectrum from turbulent jets is broadbanded, having intensity within 10 dB of its peak over two decades in frequency. The role of turbulence scales in generating this broadbanded sound is important for several reasons, large-eddy simulation of turbulent jet noise being perhaps the most obvious. Here, the degree to which noise predictions must rely upon subgrid scale modeling of the sound sources is tied, of course, to those that make the sound. Fundamentally different modelings are needed if the only important small scales are, say, the locally largest eddies spanning the thin mixing layer near the jet's nozzle rather than the small-scale turbulence distributed throughout the jet. From a noise control perspective, the largest scales are, naturally, more amenable to control, so their relative contribution to the radiated sound in different parts of its spectrum is likewise important. The role of scales is also important in theoretical jet noise models, which typically require assumptions about the statistics of noise sources. Models for turbulence statistics are expected to be more reliable for smaller scales, which are expected to be closer to homogeneous and therefore more universal.

An interesting observation about the sound spectra from jets might also be related to the role of scales. There is strong empirical evidence that over a wide range of jet operating conditions the spectrum is well fitted by two spectral shapes.^{1,2} One has a sharper spectral peak and is more active at radiation angles closer to the jet axis. The other has a broader spectrum and a more uniform directivity. Given the

similarity of the sharply peaked spectrum's directivity to that predicted by noise models based upon instability waves,³ this component is often referred to as the large-scale turbulence spectrum. The other component is thus called the fine-scale turbulence spectrum. There is no firm theoretical footing for these designations however. Such a decomposition is particularly curious since both spectra have a similar spectral peak frequency, which seems inconsistent with the expectation that finer scales should emit higher frequencies.

Rather than disparate scales, another possible explanation for this two-component character is that the same turbulent noise sources radiate by multiple mechanisms. Goldstein and Leib⁴ showed that the vector Green's function for a causal solution of an acoustic analogy constructed for a slowly diverging mean flow has two components. Operating on the same noise sources, these Green's function components act as filters which only allow certain components of the source to radiate to the far field. The resulting spectral predictions share some of the key features of experimental observations.^{4,5} Still another possibility is that noise from the near-nozzle mixing layers and that which is generated around the closing of the potential core are somehow fundamentally different, yielding different spectra. In summary, it remains unclear whether the two-component character of the spectrum results from different scales, different radiation mechanisms from the same sources, or different noise characteristics of different portions of the jet. In this study, our focus on a mixing layer is motivated in part to avoid the additional complexity introduced by the potential core structure of a jet.

It is notoriously difficult to make any direct assessment

of the sound-generating role of turbulence scales in a jet. There exists experimental evidence that most (nearly all) of the high-frequency acoustic energy comes from near the nozzle, whereas the sources of low-frequency sound are distributed along the jet axis and peak near the end of the potential core.^{6–8} Near the nozzle, the locally largest scales are on the order of the shear layer thickness and therefore are small and expected to produce high-frequency sound. This is consistent with the view that the locally largest scales are responsible for most of the radiated sound spectrum and that it is the range of locally largest scale sizes between the nozzle lip and the close of the potential core that gives the radiated spectrum its breadth. Indeed, analysis of large-eddy simulations of jets suggest that representing the thin near-nozzle shear layers is more important than subgrid scale modeling.⁹

To examine the relation of near-field turbulence scales to sound field scales, we have designed direct numerical simulations of temporally developing mixing layers (see Sec. II). Geometrically, this configuration provides a model for the shear layers in a jet prior to the close of the potential core. The role of Reynolds number in jets has recently been investigated using large-eddy simulations.¹⁰ Our simulations are designed to avoid the additional complexities introduced by the potential core and the dissipation added to such large-eddy simulations to model (at least functionally) the cascade and dissipation of energy at unresolvable scales. Simulations of several mixing layers with increasing Reynolds numbers allow the comparison of the sound fields of flows that share the same large turbulence scales, but with an increasing range of smaller scales. Physically, the temporal mixing layer also avoids the ambiguity of spatially developing flows wherein the locally largest scales from different parts of the flow radiate simultaneously. However, this nonlocality in space is traded for nonlocality in time for a temporally developing flow. The nonstationary character of the flow also makes it more convenient to consider the spatial range of scales in the sound field rather than frequency spectra directly.

Temporally developing mixing layers are computationally convenient due to their periodicity in both the streamwise and spanwise directions and have been used in many cases to study transition and turbulence.^{11–15} However, temporally developing flows are only a model for their spatially developing counterpart, and they cannot be expected to exactly match their radiated sound.¹⁶ In some examples,^{17,18} the sound from temporally developing flows appears to be dominated by plane waves traveling perpendicular to the shear layer. This behavior is an artifact of the small size of the periodic domains in those studies. An analysis of the wave-number components of a model wave equation (see the Appendix for full details) shows that the discrete wavenumber spectrum is only fundamentally restrictive when the dominant sound wavelength is comparable to the size of the periodic domain. When the spectrum is well resolved, its evolution into the sound field matches that of the continuous spectrum case.

TABLE I. Mesh parameters for the direct numerical simulations.

Case	$(N_x \times N_y \times N_z)$	Minimum $\Delta y / \delta_m^0$	Maximum $\Delta y / \delta_m^0$
ML1	340 × 213 × 84	4.68	26.48
ML2	680 × 425 × 168	2.34	13.64
ML3	2050 × 1251 × 512	0.79	4.72
ML4	2050 × 1251 × 512	0.79	4.72

II. SIMULATION DETAILS

A. The flow and flow parameters

Four temporally developing, uniform temperature mixing layers with streamwise (x) and spanwise (z) periodicities were simulated at different Reynolds numbers. The two streams of each mixing layer shared the same ambient density, temperature, pressure, and viscosity (ρ_∞ , T_∞ , p_∞ , μ_∞) and the Prandtl number was uniformly 0.7. The four mixing layers were simulated on three meshes (see Table I) all in a computational domain of size $(L_x, L_y, L_z) = (2000, 2000, 750)\delta_m^0$, where δ_m^0 was the initial momentum thickness. The grid was stretched in the cross-stream (y) direction to cluster points in the shear region as opposed to the regions above and below the layer where high resolution was not needed. A uniform mesh was used in the periodic directions. The number of mesh points used in each simulation is tabulated in Table I along with some mesh stretching parameters. The minimum $\Delta y / \delta_m^0$ occurred on the layer centerlines ($y=0$) with a maximum on the boundaries $y = \pm 1000\delta_m^0$. The stretching was set such that the spacing changed by less than 1% point-to-point in the mixing layer.

Several definitions of Reynolds number for each simulation are listed in Table II. The simulations were set such that the initial Reynolds number of ML2 was twice that of ML1, ML3 was initially three times ML2, and ML4 was initially twice ML3.

B. Numerical methods

The Navier–Stokes equations for a compressible fluid were solved numerically without modeling assumptions. The cross-stream (y) direction had a $150\delta_m^0$ -wide absorbing buffer zone at the top and bottom of the domain to mimic an infinite domain. In this zone, the solution was damped toward a quiescent state by adding a dissipative forcing term to the right-hand side of flow equations as done by Freund,¹⁹ here with $\sigma=0.6$ using the same notation. In these buffer zones, the flow was also filtered with a low-order, low-pass filtering scheme.^{20,21} One-dimensional characteristic radiation boundary conditions²² were applied at the domain edge.

High-resolution finite-difference methods were used in the streamwise and cross-stream directions. The fourth-order spectral-like pentadiagonal compact finite-difference scheme of Lele²⁰ was used in the cross-stream direction. This scheme has coefficients that are tuned to improve resolution by sacrificing formal order. The same stencil could yield a tenth-order scheme. In the streamwise direction, a higher-resolution variant of the explicit dispersion-relation-preserving scheme of Tam and Webb²³ was used. It has a

TABLE II. Reynolds numbers of the four simulations. The final Re_{δ_m} and $Re_{\delta_{99}}$ are taken at the end of the time series.

Simulation	Initial Re_{δ_m}	Final Re_{δ_m}	Final $Re_{\delta_{99}}$	Maximum Re_{λ_x}	Maximum Re_{λ_z}
ML1	35	233	2029	148	74
ML2	69	485	4297	171	97
ML3	207	1442	12 458	292	177
ML4	414	2848	24 376	422	280

nine-point stencil and sixth-order accuracy. This explicit scheme was chosen in the streamwise direction to facilitate domain decomposition for implementation on parallel computer systems. Figure 1 shows the dispersion characteristics of the first derivative routines used. A seven-point sixth-order explicit scheme was used in both the x - and y -directions for second derivative calculations. A Fourier spectral scheme was used in the spanwise direction. The solution was advanced in time with $\Delta t = 0.27 \delta_m^0 / \Delta U$ by the seven-step Runge–Kutta scheme of Hixon *et al.*,²⁴ which was optimized for stability and accuracy.

Despite its high resolution, the highest Reynolds number mixing layer simulation (ML4) required slight stabilization. This was done by high-wavenumber filtering as is often used in conjunction with such algorithms.^{25,26} No filtering was done on the ML1, ML2, or ML3 simulations. The spanwise direction was filtered with a Fourier wavenumber cutoff filter, which removed the top 15% of wavenumbers. A filtering procedure similar to that of Visbal and Gaitonde²⁵ and Bodony and Lele²⁶ was used to filter in the streamwise and cross-stream directions. A variant of the compact pentadiagonal filter of Lele²⁰ was used. Its transfer function $T(k\Delta)$ is also shown in Fig. 1. The coefficients of the scheme were set such that $T(k\Delta) = 0.95$ at $k\Delta x / \pi = 0.85$. All flow variables of the direct numerical simulation solution were filtered in each

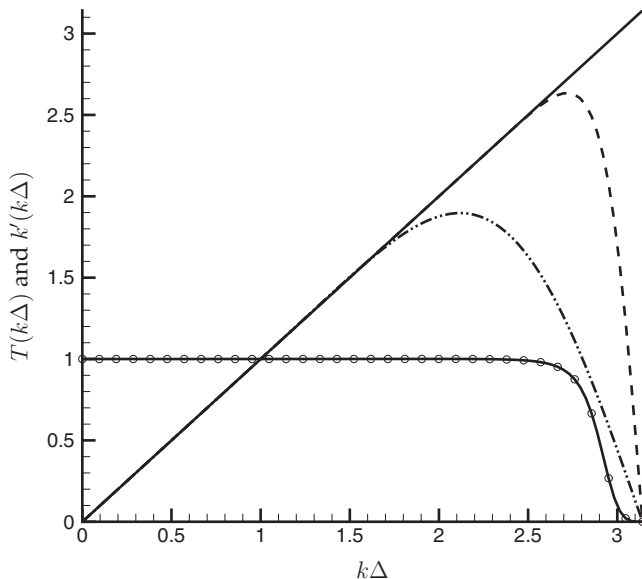


FIG. 1. Modified wavenumber of the spatial discretizations and filter transfer function: z differentiation (—); y differentiation (---); x differentiation (-·-·-); and filter $T(k\Delta)$ (-○-).

coordinate direction every five time steps, but only at 60% strength. That is, a linear combination of the filtered and unfiltered fields was used,

$$\mathbf{q}_{\text{new}} = \left[1 - \varphi \left(\frac{y}{\delta_m^0} \right) \right] \mathbf{q} + \varphi \left(\frac{y}{\delta_m^0} \right) \mathbf{q}_{\text{filt}}, \quad (1)$$

with

$$\varphi \left(\frac{y}{\delta_m^0} \right) = \frac{\varphi_{\text{max}}}{2} \left[\tanh \left(5 \frac{\left(\frac{y}{\delta_m^0} + \delta^*/2 \right)}{\delta^*/2} \right) - \tanh \left(5 \frac{\left(\frac{y}{\delta_m^0} - \delta^*/2 \right)}{\delta^*/2} \right) \right], \quad (2)$$

where $\varphi_{\text{max}} = 0.6$ and $\delta^* = 1.1 \delta_{99}(t)$. The physical width of the filtered region, δ^* , was set such that filtering effectively only had support in a region 10% larger than the 99% thickness (δ_{99}) of the layer. No filtering was applied outside of this region. It is important to note that this filtering provides mild stabilization to a highly resolved simulation and should not be regarded as a turbulence model. Its negligible effect on the resolved scales is demonstrated in Sec. III C.

C. Initial conditions

The ML3 simulation was assigned an initial streamwise mean velocity

$$U(y) = \frac{\Delta U}{2} \tanh(\sigma_y y), \quad (3)$$

where $\sigma_y = 5 / \delta_m^0$ and $\Delta U / a_\infty = 0.9$, where a_∞ is the ambient speed of sound. The Mach number of the top stream was $M_1 = +0.45$ and the bottom was $M_2 = -0.45$. The temperature was the same in both streams. No mean flow was specified in the y or z directions. The turbulence was seeded via a velocity potential

$$\begin{aligned} \phi(x, y, z) = & - \sum_{i,j}^{N_p} A_{ij} \cos \left(k_x^i \frac{x}{\delta_m^0} + \theta_i \right) \cos \left(k_z^j \frac{z}{\delta_m^0} + \varrho_j \right) \\ & \times e^{-(\sigma_y y^2 / \delta_m^0)} \left[\sin \left(\frac{y}{\delta_m^0} \right) + 2\sigma_y y \cos \left(\frac{y}{\delta_m^0} \right) \right]. \quad (4) \end{aligned}$$

Here θ_i and ϱ_j are random phases between zero and 2π . The mode amplitudes

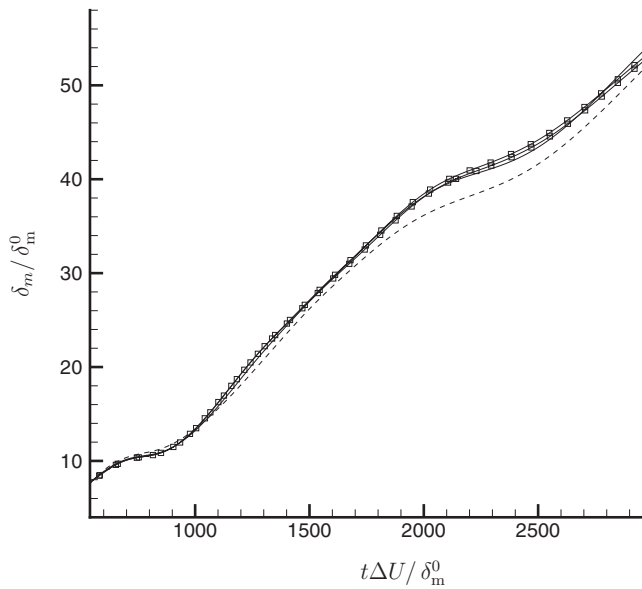


FIG. 2. Momentum thickness evolution: ML1 (----); ML2 (—); ML3 (—□—); and ML4 (—○—).

$$A_{ij} = \frac{\epsilon}{4\pi^2 k_x^i k_z^j} \quad (5)$$

had $\epsilon=0.15$ and the streamwise and spanwise wavenumbers,

$$k_x^i = \frac{2\pi i}{L_x} \delta_m^0, \quad k_z^j = \frac{2\pi j}{L_z} \delta_m^0, \quad (6)$$

gave a decaying spectrum. The longest wavelength in each direction was set to be five times the initial momentum thickness, which was equivalent to $L_x/400$ and $L_z/150$. $N_p=75$ modes were used in each direction. No initial density or pressure perturbations were imposed.

Starting from this initial condition, ML3 was simulated for $540\delta_m^0/\Delta U$ until it spread to about eight times its initial momentum thickness. At this point, significant energy was found in lower wavenumbers not excited by the initial perturbations, obvious initial transients had passed, and the layer was growing linearly in time (see Sec. III A). The ML3 field at this time was also then used as the initial flow field for the other three simulations. For the ML1 and ML2 simulations, the field was filtered and interpolated onto the smaller meshes using Fourier cutoff filters in x and z and cubic splines in y .

III. RESULTS

A. Layer growth

All of the mixing layers were simulated for $2430\delta_m^0/\Delta U$ beyond the initial condition generated in the ML3 simulation. The growth of the mixing layers is shown in Fig. 2. The layers grow about seven times their initial thickness during the simulation with the relatively viscous ML1 growing at a slightly lower rate than the others. The initial and final Reynolds numbers are reported in Table II. The layers grow at an average rate of $\delta'(t)/\Delta U=0.0187$, which is comparable to

simulations of temporal and spatial mixing layers under similar conditions¹² as well as previous experiments²⁷ of spatial mixing layers.

B. Visualization

A visualization in Fig. 3 shows the vorticity magnitude in the shear layers and pressure perturbations from p_∞ at $t=2160\delta_m^0/\Delta U$ at $z=0$. Over the range of Reynolds numbers, the pressure fields appear similar despite an obvious increase in the range of turbulence scales in the shear layer with increasing Reynolds number. Figure 3 also shows divergence of velocity in place of pressure in the sound field. Since

$$\nabla \cdot \mathbf{u} \propto \frac{dp}{dt} \quad (7)$$

in the acoustic limit, for visualization purposes this appears to augment the modestly increased range of scales (frequencies) in the sound field. The visualizations at $z=0$ are representative of each layer's large-scale structures throughout the spanwise domain. The pairing events are not localized in this direction and the structures cover almost the entire spanwise domain. No attempt was made to decorrelate the turbulent structures in this direction.

C. Energy spectra

One-dimensional turbulence energy spectra calculated on the centerline are shown in Fig. 4 at $t=2160\delta_m^0/\Delta U$. The mixing layers never become statistically stationary, but by this point in time only the peak wavenumber is changing substantially, progressing to lower wavenumbers as the layer grows. This suggests that the turbulence is fully developed. The spectra show that all of the mixing layers are well resolved with the streamwise spectra dropping at least eight decades and the spanwise spectra dropping at least seven. For the stabilized ML4 simulation, the vertical line in Fig. 4(a) labeled “ T_{999} ” marks the wavenumber for which the stabilizing filter's transfer function was $T(k_x\delta_m)=0.999$. The sudden drop in the spanwise spectra of ML4 in Fig. 4(b) shows the effect of the Fourier cutoff filter used in that direction. As expected, the spectra are similar in the energy of the largest wavelengths.

The resolution of the turbulence is far better than typical large-eddy simulations and the stabilizing filtering is restricted to only the highest wavenumbers. Assessing the effects of the filter on the resolved scales is needed. This is particularly important since it provides no physical model for the unresolved scales and would therefore be expected to fail as a subgrid scale model if applied closer to the energetic scales. We regard it as providing a minimal amount of numerical stabilization to a direct numerical simulation. To assess the effect of the filter on the turbulence in ML4, an additional simulation was done. Given the well-resolved direct numerical simulation of ML3, its field was filtered and interpolated onto a mesh with half the points in each direction ($1025 \times 626 \times 256$) in the same manner as for the ML1

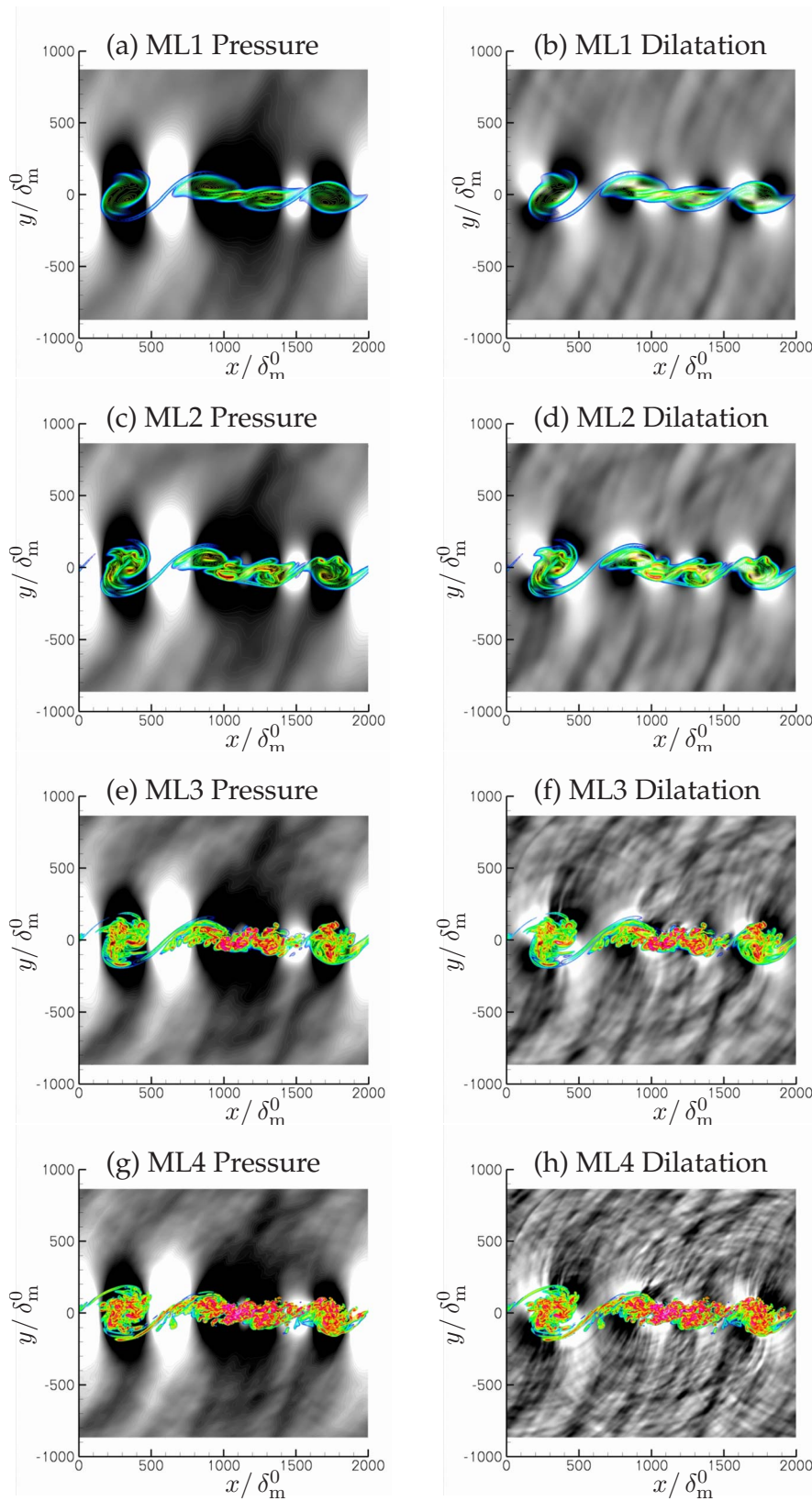
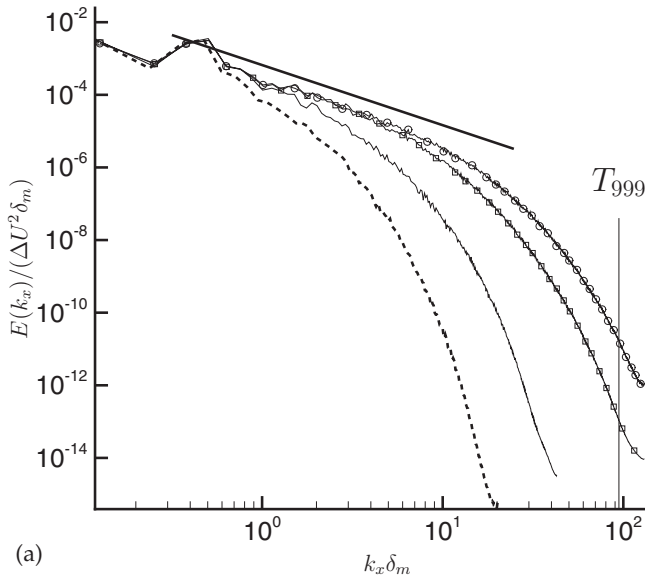


FIG. 3. (Color online) Pressure, dilatation ($\nabla \cdot \mathbf{u}$) and vorticity magnitude visualizations.

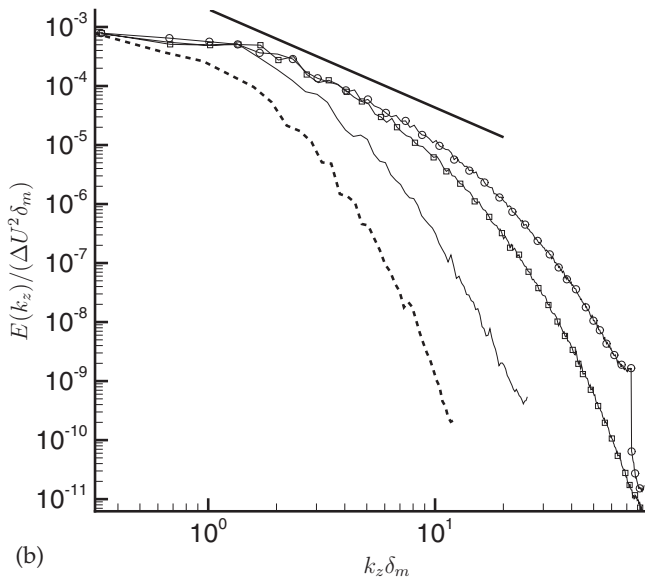
and ML2 initial conditions. The Reynolds number was left unchanged but the same filtering procedure used for the ML4 simulation was applied. This allowed for a direct comparison of filtered fields with the corresponding direct numerical simulations which should reveal the same errors as caused by the stabilization of ML4. The energy spectra and pressure

spectra of the two cases are compared in Fig. 5 and show essentially no difference up to the T_{999} point.

Only ML3 and ML4 have spectra suggestive of an inertial range, and their spectra appear to collapse in this region (see Fig. 6) when subjected to scaling via the streamwise Taylor microscale



(a)



(b)

FIG. 4. One-dimensional kinetic energy spectra at $y=0$ in the (a) x and (b) z directions with ML1 (----); ML2 (—); ML3 (–□–); and ML4 (–○–). The straight solid lines have a slope of $-5/3$.

$$\lambda_x(t) = \left(\frac{\overline{u'u'}}{\frac{\partial u'}{\partial x} \frac{\partial u'}{\partial x}} \right)^{1/2}, \quad (8)$$

which is computed on the mixing layer centerline and where $(\overline{\quad})$ denotes averaging in the x - and z -directions. The spectra of ML1 and ML2 do not collapse with this scaling, which is consistent with their apparent lack of an inertial range. Similar results are found with the spanwise velocity spectra (not shown) when scaled by λ_z , the spanwise Taylor microscale defined in the same manner as Eq. (8). Kolmogorov scaling collapses the streamwise and spanwise spectra of ML3 and ML4 at high wavenumbers.²⁸

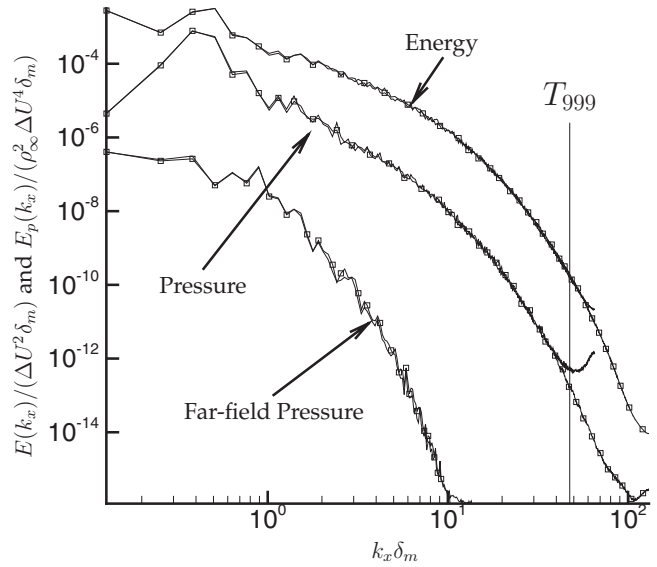


FIG. 5. One-dimensional x -direction energy and pressure spectra computed at $y=0$ and $y=-850\delta_m^0$ (denoted as “far-field pressure”): stabilized coarser mesh simulation (—) (see text) and ML3 (–□–).

D. Pressure spectra

To investigate the increasing range of turbulence scales at higher-Reynolds numbers, we compare near- and far-field pressure spectra. All spectra were calculated at $t = 2160\delta_m^0 / \Delta U$, the same time of the simulation as the energy spectra presented in Sec. III C and visualizations in Sec. III B. One-dimensional pressure spectra in the streamwise and spanwise directions were calculated at $y=0$ and $|y| = 850\delta_m^0$. The pressure spectra at $y=-850\delta_m^0$ and $y=850\delta_m^0$ were computed and averaged together to provide a measure of sound in the far field. Confirmation of the far field was attained via an extrapolation using data from the $y=-550\delta_m^0$ plane from the direct numerical simulations as a boundary condition for an Euler equation solution beyond the Navier–Stokes domain.

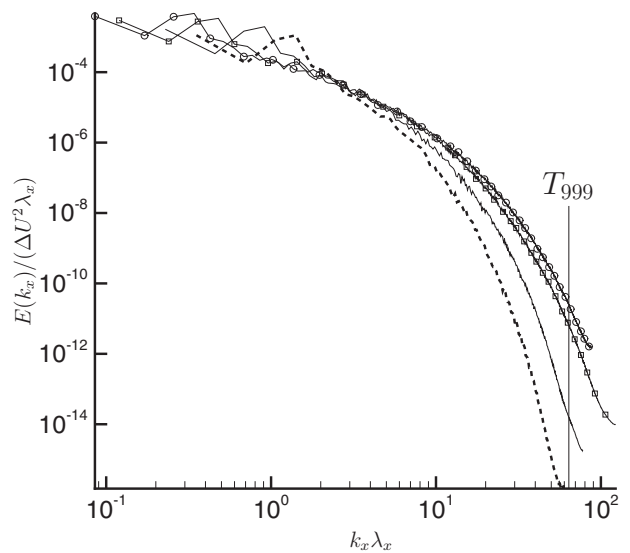


FIG. 6. One-dimensional streamwise velocity spectra at $y=0$ scaled by the Taylor microscale, λ_x : ML1 (----); ML2 (—); ML3 (–□–); and ML4 (–○–).

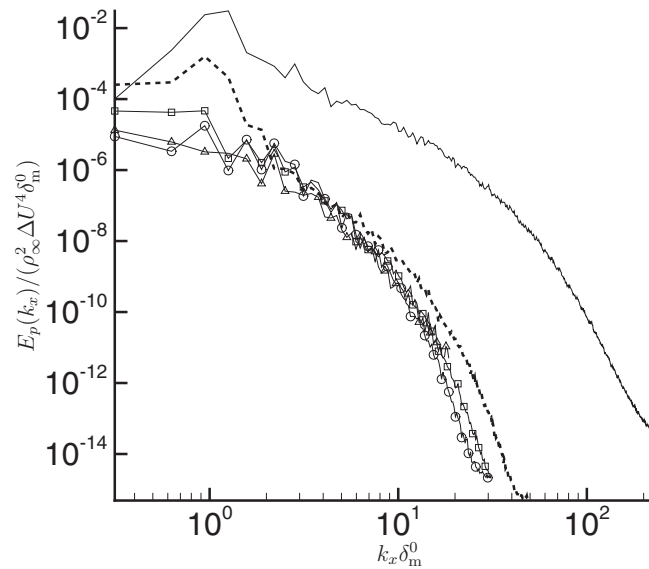
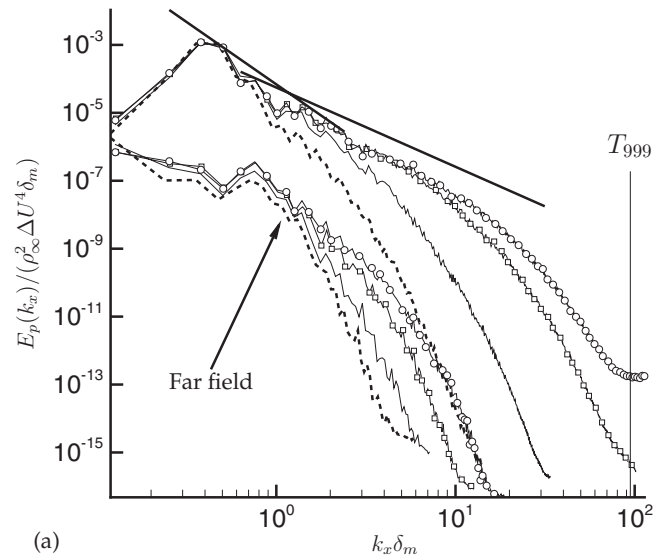


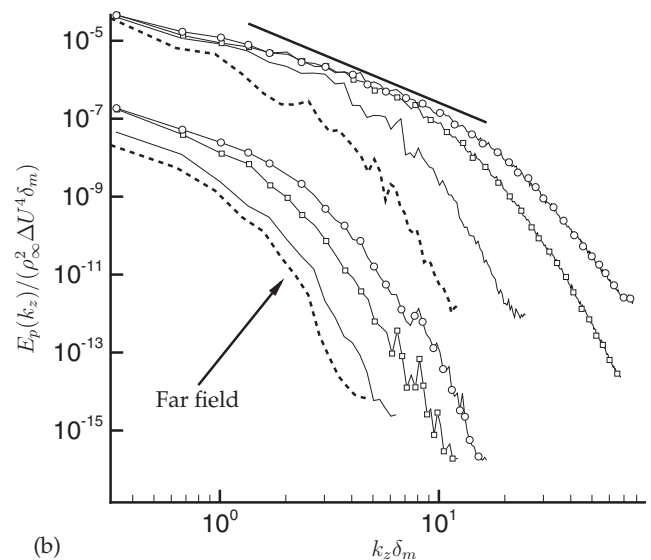
FIG. 7. One-dimensional x -direction pressure spectra of ML3 simulation at several y locations at propagation adjusted times. $y=0$ (—); $y=-250\delta_m^0$ (---); $y=-550\delta_m^0$ (-□-); $y=-850\delta_m^0$ (-○-); and $y=-1850\delta_m^0$ (-△-).

This result is shown in Fig. 7 for one-dimensional streamwise pressure spectra of ML3 at several cross-stream locations below the shear layer. The propagation-time adjusted far-field pressure spectra at $y=-550\delta_m^0$ and $y=-850\delta_m^0$ calculated by the direct numerical simulations showed no significant differences with the spectrum at $y=-1850\delta_m^0$. The Euler solver used a smaller mesh since it was far from the shear layer and therefore the highest wavenumber in Fig. 7 is less than the other spectra obtained from the direct numerical simulation data. A slight variation is seen from the $y=-250\delta_m^0$ location to those further away. The structures of the mixing layer grow into this region at this time in the simulation which is seen in the low wavenumber components of Fig. 7. These results also justify the utility of the current direct numerical simulations of temporal mixing layers to study far-field sound. As per the discussion in Sec. I and the Appendix, the energy in any particular streamwise (and spanwise, not shown) wavenumbers do not decay away from $y=-250\delta_m^0$ and therefore do not result in purely planar waves in the far field.

Figure 8(a) shows the streamwise near- and far-field pressure spectra scaled by the momentum thickness. The lowest wavenumbers of all four mixing layers scale with the momentum thickness, as was the case with the energy spectra. The effect of Reynolds number is similarly clear here. ML1 and ML2 depart near $k_x\delta_m \approx 1$, whereas ML3 and ML4 continue on together at a constant slope until $k_x\delta_m \approx 10$ where the ML3 curve begins to decay. This region of constant slope corresponds to the $k^{-7/3}$ inertial range scaling for mean-square pressure fluctuations for homogeneous turbulence.²⁹ George *et al.*³⁰ extended the scaling analysis to turbulent shear flows and suggested a switch from $k^{-7/3}$ (turbulence-turbulence) to $k^{-11/3}$ (turbulence-mean shear) at lower wavenumbers. These scalings appear to explain a kink in the spectra of an axisymmetric, incompressible jet³⁰ and a similar change in slope has been observed in large-eddy



(a)



(b)

FIG. 8. One-dimensional pressure spectra at $y=0$ and $y=\pm 850\delta_m^0$ (denoted as “far field”): (a) x -direction, with straight solid lines having slopes $-11/3$ and $-7/3$, and (b) z -direction with the straight solid line having slope $-7/3$. Curves designate: ML1 (---); ML2 (—); ML3 (-□-); and ML4 (-○-).

simulations of compressible jets.²⁶ In the current study, ML3 and ML4 exhibit the $-7/3$ slope over almost a decade of wavenumbers and a kink in the spectra shows the possible transition to the $-11/3$ slope, although the limited size of the computational domain prevents forming any strong conclusions in this regard.

Far-field streamwise spectra are also shown in Fig. 8(a). When scaled by the layer thickness, ML2, ML3, and ML4 collapse well in lower wavenumbers, with ML1 showing slightly lower values. The far-field spectra of ML2, ML3, and ML4 all diverge at about the same wavenumber—near the wavenumber of the beginning of the apparent near-field inertial range in the centerline spectra. The far-field spectra also decay much faster after the beginning of the inertial range than the near-field spectra, especially for the ML3 and ML4 cases. Figure 8(b) shows the spanwise near- and far-

field pressure spectra scaled by the layer momentum thickness. The far-field spectra decay in the same manner as the streamwise far-field spectra—well before the centerline spectra decay. However, in contrast to the streamwise spectra, the spanwise spectra do not collapse in any region of wavenumbers when scaled by the layer thickness.

The narrow character of the far-field spectra compared to the source spectra in the near field at $y=0$ is expected from the acoustic analogy of Lighthill.³¹ It is well known that only components of the source with streamwise supersonic phase velocity are capable of radiating to the far field.^{32–35} The radiation-capable portion of a $k-\omega$ plane and the turbulence spectrum in this same plane is expected of itself to limit the radiation to the far field, effectively narrowing the far-field spectra.

Pressure waves may be attenuated as they travel from their source due to the effects of viscosity. The extent of the dissipation is related to the distance the waves have traveled, the Reynolds number, and the frequency/wavenumber of the disturbances. Based on the standard estimates (e.g., Pierce³⁶) under the assumption of plane waves emitted from the shear layer, it can be shown that the viscous attenuation is expected to be negligible for the wavenumber ranges of interest at $|y|=850\delta_m^0$ for all of the mixing layers.²⁸

Figure 9(a) shows the streamwise pressure spectra scaled by the Taylor microscale, λ_x . The near-field spectra in the streamwise direction collapse in a similar manner as the energy spectra. ML3 and ML4 scale together for a decade in wavenumber. The far-field spectra show that all the spectra are moved together for the ML3 and ML4 cases over almost the entire spectrum except at the lowest wavenumbers, where it scaled well with the layer thickness, δ_m . The lower Reynolds number cases do not collapse with the higher cases. The centerline spanwise spectra in Fig. 9(b) show the ML3 and ML4 cases collapsing in a similar fashion as the streamwise. The maximum values of the spanwise Taylor Reynolds number Re_{λ_z} are reported in Table II and are all 1.5–2 times smaller than their streamwise counterparts. However, the ML2 case in the spanwise direction also collapses well with the higher-Reynolds-number simulations.

E. Acoustic power and energy

The net radiated acoustic power (area-integrated acoustic intensity) is defined as

$$\mathcal{P}(t) = \frac{1}{\rho_\infty a_\infty} \int_0^{L_z} \int_0^{L_x} [p(x, y_b, z, t) - \bar{p}(y_b, t)]^2 dx dz, \quad (9)$$

where $y_b = \pm 850\delta_m^0$, the location of the far-field spectra calculated in Sec. III D. The curves of $\mathcal{P}(t)$ at $y=-850\delta_m^0$ and $y=850\delta_m^0$ have been averaged together and are shown in Fig. 10. As smaller scales are introduced to the flow by increasing the Reynolds number, the net effect on the acoustic power is minimal. The curves of $\mathcal{P}(t)$ are coincident at the beginning due to all of the mixing layers being started from the same initial condition. As the Reynolds number is doubled from ML1 to ML2, there is a marked increase in $\mathcal{P}(t)$. ML1's contribution follows the same trends as the other three layers at a lower magnitude, but near the end of the time series

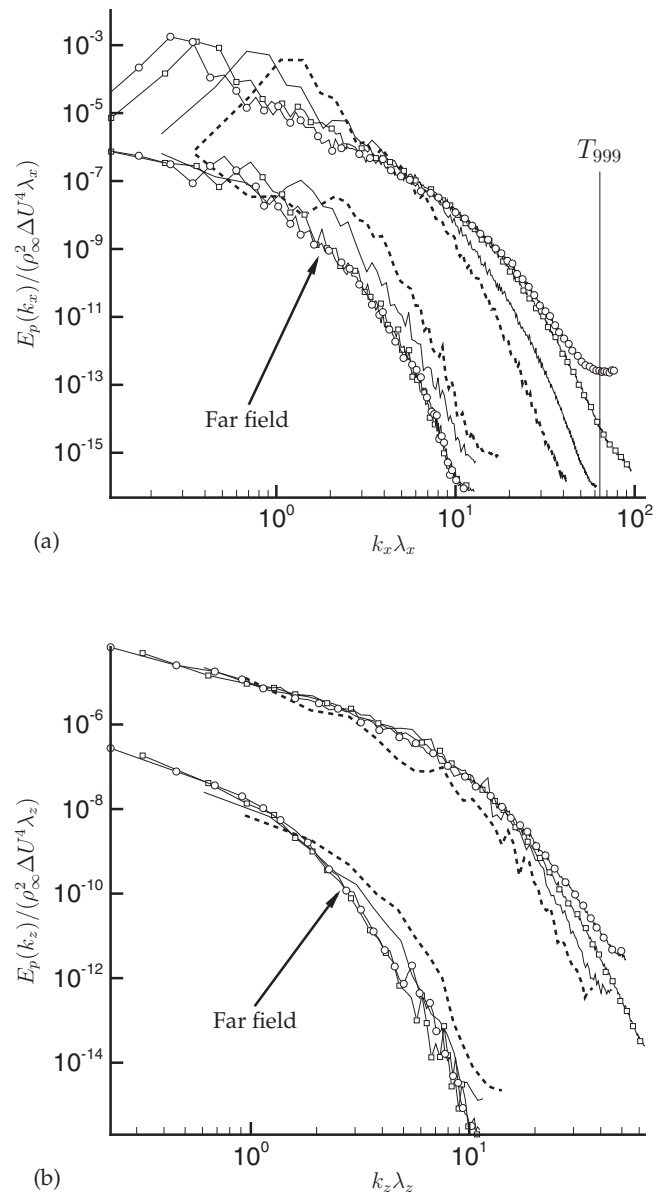


FIG. 9. One-dimensional pressure spectra at $y=0$ and at $y = \pm 850\delta_m^0$: (a) x -direction scaled by the streamwise Taylor microscale λ_x , and (b) z -direction scaled by the spanwise Taylor microscale λ_z . Curves indicate: ML1 (----); ML2 (—); ML3 (□); and ML4 (○).

joins the other curves. At $t=2810\delta_m^0/\Delta U$ where the ML1 curve joins the others, $Re_{\delta_m} = 215$ for ML1, which is near the initial value of ML3 (see Table II). The same trend is true for ML2, which initially is far from the almost coincident ML3 and ML4 curves, but joins them in almost half the time as ML1. The doubling of Reynolds number from ML3 to ML4 has little effect on the values of $\mathcal{P}(t)$.

To quantify this result further, integrating with respect to time gives

$$\mathcal{E}_{A \rightarrow B} = \int_{t=A}^{t=B} \mathcal{P}(t) dt, \quad (10)$$

the total acoustic energy through the $y = \pm 850\delta_m^0$ planes over the time horizon of the four simulations. Four points of interest in the time series are marked in Fig. 10. Point A is the

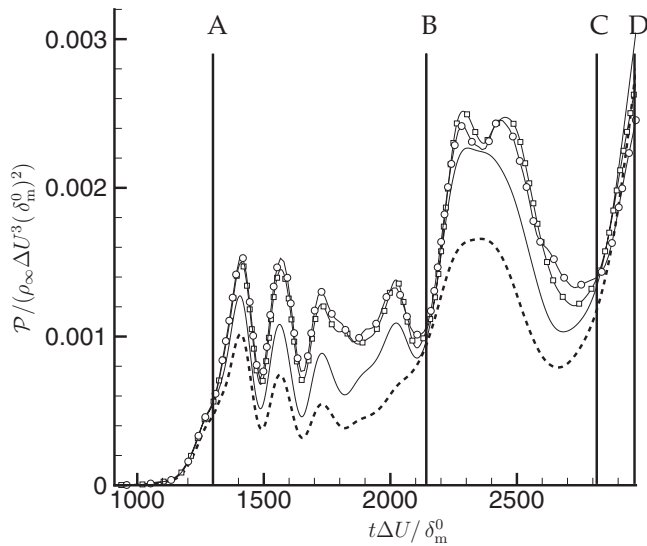


FIG. 10. Acoustic power $\mathcal{P}(t)$ at $y=y_b$; ML1 (----); ML2 (—); ML3 (—□—); and ML4 (—○—).

approximate location where the four curves begin to “forget” the initial condition ($t=1295\delta_m^0/\Delta U$). Point B is the location where ML2’s curve joins ML3 and ML4 ($t=2140\delta_m^0/\Delta U$). Point C is the location where the same happens for ML1 ($t=2810\delta_m^0/\Delta U$), and point D marks the end of the time series ($t=2970\delta_m^0/\Delta U$). Table III shows the results of integrating between points $A \rightarrow D$, $B \rightarrow E$, and $C \rightarrow D$.

The integration from $A \rightarrow D$ shows that ML3 and ML4 have equivalent \mathcal{E} despite showing minor visual differences in $\mathcal{P}(t)$ in Fig. 10. This suggests that the additional small scales included in ML4 had little contribution to the net acoustic energy radiated. As ML2 grows in time and reaches a Reynolds number similar to the initial Reynolds number of ML3 at point B, the results of the integration from $B \rightarrow D$ show ML2 being roughly the same despite differences in the curves of $\mathcal{P}(t)$. From $C \rightarrow D$, where all of the curves lie near each other, the integrations show similar values of energy for each mixing layer. For $\text{Re}_{\delta_m} \gtrsim 300$ the simulations seem to radiate the same net acoustic energy.

F. The role of vortex pairing

The distinct peaks and valleys of the acoustic power $\mathcal{P}(t)$ in Fig. 10 do not seem to correspond to any particular events, such as vortex pairings, in the near field. Several studies of harmonically excited flows have shown noise due to vortex pairing in free shear flows.^{17,18,37–40} However, Wei and Freund⁴¹ showed using an adjoint-based control optimization procedure that the sound from a randomly excited (nonhar-

monic) two-dimensional mixing layer could be significantly suppressed without altering the vortex pairing dynamics.

The pairing history in the present flows was quantified by counting the low pressure regions (where $p-p_\infty < 0$) along the streamwise direction at $y=z=0$. All spanwise locations showed similar behavior. A vortex structure corresponds to each of these regions and pairings occur when regions converge. Figure 11 shows the decreasing number of structures versus time for the four mixing layers. The gray boxes in Fig. 11 surround the four main peaks of $\mathcal{P}(t)$ in Fig. 10 at times $t=(1413, 1573, 2025, \text{ and } 2390)\delta_m^0/\Delta U$, shifted to approximate the retarded time factor between $y=0$ and $|y|=850\delta_m^0$. There appears to be no pairing pattern that corresponds to the fluctuations in radiated energy. Other measures of vortex pairing noise also show no conclusive role of pairing in this flow and are to be reported elsewhere.²⁸

G. Far-field frequency spectra

It is of course challenging to compute frequency spectra for time-developing flows, but the time spectra show essentially the same behavior as the wavenumber spectra. Far-field frequency spectra of the four mixing layers at $y=-850\delta_m^0$ are presented in Fig. 12. To compute the spectra the time series of pressure data between $t=765\delta_m^0/\Delta U$ and $t=2970\delta_m^0/\Delta U$ was used. These times corresponded to slightly after pressure fluctuations from the initial field of the mixing layers reached the $y=-850\delta_m^0$ plane and to the end of the data set, respectively. Spectra were calculated at every sixth data point in x and every other data point in z , averaged together, and binned to create the 1/3-octave averaged spectra shown. The data sets were windowed with a Blackman (triangle) function.

All of the mixing layers have a broadband of frequencies, but similar magnitude only in the lowest frequencies, with ML3 and ML4 being almost identical. A rapid decay is seen after $\omega=0.01\Delta U/\delta_m^0$ especially in the low Reynolds number cases. ML3 and ML4 follow each other closely until about $\omega=0.04\Delta U/\delta_m^0$, where both have decayed three decades. That the simulations are similar in the lowest frequencies confirms again that their shared turbulence scales, namely, the largest scales, are responsible for the majority of the sound emission. For ML3 and ML4, the addition of the smaller scales appears to only affect frequencies above $\omega=0.04\Delta U/\delta_m^0$ at magnitudes significantly below the levels of the lower frequencies. The trend is more evident when comparing ML1 and ML2 to the higher-Reynolds-number simulations at higher frequencies.

IV. CONCLUSIONS AND DISCUSSION

The far-field sound is seen to have a streamwise wavenumber spectrum that is invariant to Reynolds number over the same range of wavenumbers as the near-field turbulence. Nearly all the radiated acoustic energy is in this range, which is consistent with Lighthill’s statistical estimates of stress-tensor correlations.⁴² Based on the net radiated power, more than 85% of the acoustic energy that would apparently be radiated in the high-Reynolds-number limit is radiated for

TABLE III. Net acoustic energy \mathcal{E} between labeled points in Fig. 10.

	$\mathcal{E}_{A \rightarrow D}$	$\mathcal{E}_{B \rightarrow D}$	$\mathcal{E}_{C \rightarrow D}$
ML1	1.596	1.102	0.278
ML2	2.110	1.412	0.312
ML3	2.458	1.557	0.299
ML4	2.480	1.538	0.274

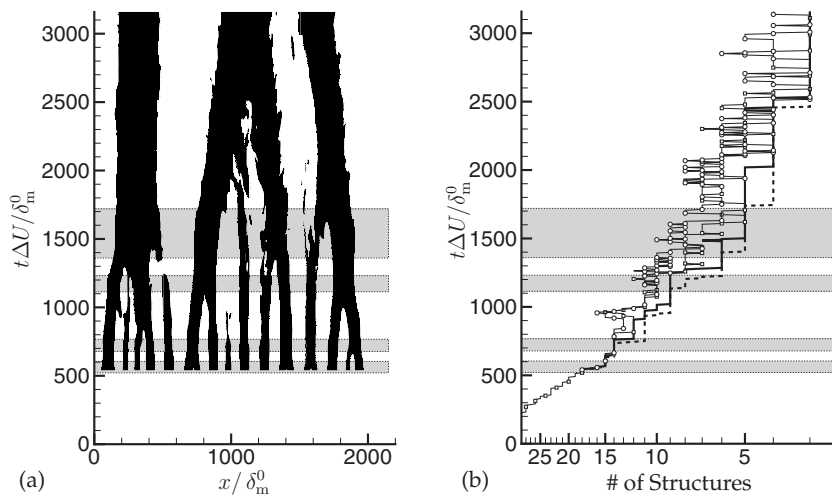


FIG. 11. (a) Pressure evolution at $y = z = 0$ of the ML4 mixing layer. Black denotes $(p - p_\infty)/(\rho_\infty \Delta U^2) < 0$ and white denotes $(p - p_\infty)/(\rho_\infty \Delta U^2) > 0$. (b) Number of large-scale structures showing the progression of pairing events at $y = z = 0$ in the ML1 (----), ML2 (—), ML3 (-□-), and ML4 (-○-) mixing layers. The horizontal axis is shown with a logarithmic scale. Propagation-time adjusted time intervals surrounding several peaks of acoustic power in Fig. 10 are shaded in gray in both (a) and (b).

$Re_{\delta_m} \approx 300$. This result suggests that there should be a low burden in large-eddy simulations to represent noise from turbulence scales that are not explicitly represented, although any importance weighting of the spectrum such as for gauging annoyance could, of course, complicate this conclusion. This is also consistent with the conclusions of Bodony and Lele⁹ deduced from the relative success of large-eddy simulations. They conclude that the fidelity of the radiated sound prediction is most dependent upon representing the locally largest turbulence scales near the nozzle. The frequency spectra we were able to estimate for the nonstationary flow suggest a similar behavior. In contrast to large-eddy simulation, modeling approaches that require assumptions about the statistical properties of the turbulence (e.g., isotropic, homogeneous,⁴³ and axisymmetric⁴⁴) will be most challenged by the need to model the statistics of the largest scales, which are never universal.

Interestingly, the spanwise structure of the sound field shows no similar low wavenumber collapse despite the low wavenumber Reynolds number insensitivity of the spanwise

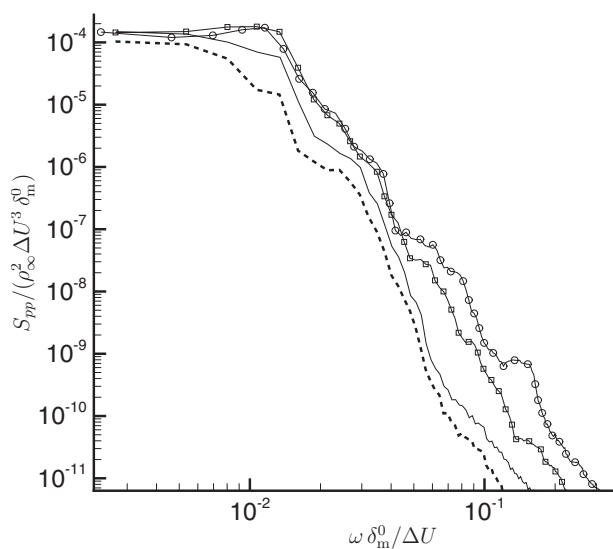


FIG. 12. 1/3-octave frequency spectra at $y = -850\delta_m^0$; ML1 (----); ML2 (—); ML3 (-□-); and ML4 (-○-).

spectra in the near field. This is consistent with the notion that the largest instability wave structures in the flow radiate in a special fashion as they propagate downstream. This line of thinking is the basis for the designation of the more peaked empirical sound spectrum component as being associated with the large turbulence structures¹ and consistent with detailed analysis of the role of instabilities in generating far-field sound.⁴ In simple analytical models, instability wave structures can have a highly downstream directive (so-called superdirective) character.⁴⁵ This type of directivity and near-field sources have been deduced via spectral analysis of low-Reynolds-number jet turbulence.³⁵

The spectra for the Reynolds-number-sensitive higher wavenumbers of the streamwise spectra and all the wavenumbers for the spanwise spectra collapse reasonably well with the turbulence microscale scaling. This suggests that only this low-energy part of the sound derives from scales smaller than the most energetic. Although the acoustic energy in this range is much less than the spectral peaks, it could conceivably be important in some cases when weighting the sound for human annoyance. The highest two Reynolds number mixing layers, both of which showed evidence of an inertial range, show better collapse of their spectra via this scaling. There is no evidence that viscosity itself directly affects any part of the radiated sound spectra.

ACKNOWLEDGMENTS

This work was supported in part by the (U.S.) Department of Energy and NASA Grant No. NNX07AC86A. It was first presented at a symposium honoring Professor John Kim. J.B.F. is ever grateful for John's unwavering encouragement, sound advice, and friendship.

APPENDIX: DECAY OF NONPLANAR WAVES IN PERIODIC DOMAINS

Lele and Ho¹⁷ analyzed a two-dimensional streamwise periodic domain via a model wave equation, which we generalize here to include the spanwise (z) coordinate direction. A disturbance $\phi(x, y, z, t)$ due to arbitrary sound sources Q is governed by

$$\left(\frac{\partial}{\partial t} + U\frac{\partial}{\partial x}\right)^2 \phi - a_\infty^2 \nabla^2 \phi = Q(x, y, z, t), \quad (\text{A1})$$

where U is the mean velocity of the flow in the x direction. A Fourier transform in x and z yields an advected Klein-Gordon equation

$$\left(\frac{\partial}{\partial t} + ik_x U \frac{\partial}{\partial x}\right)^2 \hat{\phi} - a_\infty^2 \left(\frac{\partial^2}{\partial y^2} - (k_x^2 + k_z^2)\right) \hat{\phi} = \hat{Q}(k_x, y, k_z, t). \quad (\text{A2})$$

Note that the same equation as the above results regardless of whether the domain is periodic with discrete wavenumbers $k_x^n = 2\pi n/L_x$ and $k_z^m = 2\pi m/L_z$, or if the wavenumber spectrum is continuous. The free space Green's function of Eq. (A2) is

$$G(y, t; y', t') = \frac{1}{2} e^{-ik_x U(t-t')} H\left[t - t' - \frac{|y - y'|}{a_\infty}\right] \times J_0\left[ka_\infty \sqrt{(t-t')^2 - \frac{(y-y')^2}{a_\infty^2}}\right], \quad (\text{A3})$$

where $k = \sqrt{k_x^2 + k_z^2}$ and H is the Heaviside function. The solution of Eq. (A2) is

$$\hat{\phi}(k_x, y, k_z, t) = \int_{t'=-\infty}^{\infty} \int_{y'=-\infty}^{\infty} \hat{Q}(k_x, y, k_z, t') G(y, t; y', t') dy' dt'. \quad (\text{A4})$$

Since for any k the sound field behavior is independent of whether or not the domain is periodic—whether or not the spectrum is discrete or continuous—any effect of the periodicity is not due to the periodic images *per se*. When the discrete spectrum is a good model for the infinite-domain continuous spectrum (that is, it retains adequate wavenumber resolution), we do not expect any direct effects of the periodicity. This amounts to having a sufficiently large periodic domain size.

A $k=0$ dominance in the sound field (e.g., Lele and Ho¹⁷) can result from a strong correlation on the scale of the computational box, which is equivalent to coarse resolution of the low wavenumbers. When the sound wavelength is comparable to the periodic box size, only $k=0$ radiation is possible since this is the only discrete wavenumber that satisfies the $|\omega| > |k|a_\infty$ condition for radiation.

¹C. K. W. Tam and L. Auriault, "Jet mixing noise from fine-scale turbulence," *AIAA J.* **37**, 145 (1999).

²K. Viswanathan, "Analysis of the two similarity components of turbulent mixing noise," *AIAA J.* **40**, 1735 (2002).

³C. K. W. Tam, M. Golebiowski, and J. M. Seiner, "On the two components of turbulent mixing noise from supersonic jets," Proceedings of the Second AIAA/CEAS Aeroacoustics Conference, State College, PA, May 1996, AIAA Paper No. 1996-1716.

⁴M. Goldstein and S. J. Leib, "The role of instability waves in predicting jet noise," *J. Fluid Mech.* **525**, 37 (2005).

⁵M. Goldstein, "Ninety-degree acoustic spectrum of a high speed air jet," *AIAA J.* **43**, 96 (2005).

⁶S. Narayanan, T. Barber, and D. R. Polak, "High subsonic jet experiments: Turbulence and noise generation studies," *AIAA J.* **40**, 430 (2002).

⁷S. R. Venkatesh, D. R. Polak, and S. Narayanan, "Beamforming algorithm for distributed source localization and its application to jet noise," *AIAA J.* **41**, 1238 (2003).

⁸M. Harper-Bourne, "Radial distribution of jet noise sources using far-field microphones," Proceedings of the Fourth AIAA/CEAS Aeroacoustics Conference, Toulouse, France, June 1998, AIAA Paper No. 1998-2357.

⁹D. J. Bodony and S. K. Lele, "Current status of jet noise predictions using large-eddy simulation," *AIAA J.* **46**, 364 (2008).

¹⁰C. Bogey and C. Bailly, "Investigation of downstream and sideline subsonic jet noise using large eddy simulation," *Theor. Comput. Fluid Dyn.* **20**, 23 (2006).

¹¹N. D. Sandham and W. C. Reynolds, "Three-dimensional simulations of large eddies in the compressible mixing layer," *J. Fluid Mech.* **224**, 133 (1991).

¹²M. Rogers and R. Moser, "Direct simulation of a self-similar turbulent mixing layer," *Phys. Fluids* **6**, 903 (1994).

¹³A. W. Vreman, N. D. Sandham, and K. H. Luo, "Compressible mixing layer growth rate and turbulence characteristics," *J. Fluid Mech.* **320**, 235 (1996).

¹⁴J. B. Freund, S. K. Lele, and P. Moin, "Compressibility effects in a turbulent annular mixing layer: Part I. Turbulence and growth rate," *J. Fluid Mech.* **421**, 229 (2000).

¹⁵C. Pantano and S. Sarkar, "A study of compressibility effects in the high-speed turbulent shear layer using direct numerical simulation," *J. Fluid Mech.* **451**, 329 (2002).

¹⁶E. J. Avital, N. D. Sandham, and K. H. Luo, "Mach wave radiation by mixing layers: Part I. Analysis of the sound field," *Theor. Comput. Fluid Dyn.* **12**, 73 (1998).

¹⁷S. K. Lele and C. M. Ho, private communication (1993).

¹⁸V. Fortuné, E. Lamballais, and Y. Gervais, "Noise radiated by a non-isothermal, temporal mixing layer. Part I: Direct computation and prediction using compressible DNS," *Theor. Comput. Fluid Dyn.* **18**, 61 (2004).

¹⁹J. B. Freund, "Proposed inflow/outflow boundary condition for direct computation of aerodynamic sound," *AIAA J.* **35**, 740 (1997).

²⁰S. Lele, "Compact finite-difference schemes with spectral-like resolution," *J. Comput. Phys.* **103**, 16 (1992).

²¹T. Colonius, S. K. Lele, and P. Moin, "Boundary-conditions for direct computation of aerodynamic sound generation," *AIAA J.* **31**, 1574 (1993).

²²K. Thompson, "Time-dependent boundary-conditions for hyperbolic systems," *J. Comput. Phys.* **68**, 1 (1987).

²³C. Tam and J. Webb, "Dispersion-relation-preserving finite-difference schemes for computational acoustics," *J. Comput. Phys.* **107**, 262 (1993).

²⁴R. Hixon, V. Allampali, M. Nallasamy, and S. Sawyer, "High-accuracy large-step explicit Runge-Kutta (HALE-RK) schemes for computational aeroacoustics," Proceedings of the 44th AIAA Aerospace Sciences Meeting and Exhibit, Reno, Nevada, January 2006, AIAA Paper No. 2006-797.

²⁵M. Visbal and D. Gaitonde, "On the use of higher-order finite-difference schemes on curvilinear and deforming meshes," *J. Comput. Phys.* **181**, 155 (2002).

²⁶D. J. Bodony and S. K. Lele, "On using large-eddy simulation for the prediction of noise from cold and heated turbulent jets," *Phys. Fluids* **17**, 085103 (2005).

²⁷J. H. Bell and R. D. Mehta, "Development of a two-stream mixing layer from tripped and untripped mixing layers," *AIAA J.* **28**, 2034 (1990).

²⁸R. R. Kleinman, "On the turbulence-generated sound and control of compressible mixing layers," Ph.D. thesis, University of Illinois, 2008.

²⁹G. K. Batchelor, "Pressure fluctuations in isotropic turbulence," *Proc. Cambridge Philos. Soc.* **47**, 359 (1951).

³⁰W. K. George, P. D. Beuther, and R. E. Arndt, "Pressure spectra in turbulent free shear flows," *J. Fluid Mech.* **148**, 155 (1984).

³¹M. J. Lighthill, "On sound generated aerodynamically: I. General theory," *Proc. R. Soc. London, Ser. A* **211**, 564 (1952).

³²J. E. Pflowcs Williams, "The noise from turbulence convected at high speed," *Philos. Trans. R. Soc. London, Ser. A* **255**, 469 (1963).

³³D. G. Crighton, "Excess noise field of subsonic jets," *J. Fluid Mech.* **56**, 683 (1972).

³⁴M. E. Goldstein, W. Braun, and J. J. Adamczyk, "Unsteady-flow in a supersonic cascade with strong in-passage shocks," *J. Fluid Mech.* **83**, 569 (1977).

³⁵J. B. Freund, "Noise sources in a low-Reynolds-number turbulent jet at Mach 0.9," *J. Fluid Mech.* **438**, 277 (2001).

³⁶A. D. Pierce, *Acoustics: An Introduction to its Physical Principles and Applications* (Acoustical Society of America, Woodbury, NY, 1989).

³⁷J. Bridges and F. Hussain, "Direct evaluation of aeroacoustic theory in a jet," *J. Fluid Mech.* **240**, 469 (1992).

³⁸T. Colonius, S. K. Lele, and P. Moin, "Sound generation in a mixing layer," *J. Fluid Mech.* **330**, 375 (1997).

- ³⁹J. Laufer and T. Yen, "Noise generation by a low-Mach-number jet," *J. Fluid Mech.* **134**, 1 (1983).
- ⁴⁰J. E. Ffowcs Williams and A. J. Kempton, "Noise from large-scale structure of a jet," *J. Fluid Mech.* **84**, 673 (1978).
- ⁴¹M. J. Wei and J. B. Freund, "A noise-controlled free shear flow," *J. Fluid Mech.* **546**, 123 (2005).
- ⁴²M. J. Lighthill, "An estimate of the covariance of T_{xx} without using statistical assumptions," in *Computational Aeroacoustics*, edited by J. C. Hardin and M. K. Hussaini (Springer-Verlag, New York, 1992), Appendix 1.
- ⁴³M. E. Goldstein and B. M. Rosenbaum, "Effect of anisotropic turbulence on aerodynamic noise," *J. Acoust. Soc. Am.* **54**, 630 (1973).
- ⁴⁴A. Khavaran, "Role of anisotropy in turbulent mixing noise," *AIAA J.* **37**, 832 (1999).
- ⁴⁵D. G. Crighton and P. Huerre, "Shear-layer pressure-fluctuations and superdirective acoustic sources," *J. Fluid Mech.* **220**, 355 (1990).